Physics and Chemistry of Minerals
https://doi.org/10.1007/s00269-018-0993-7

ORIGINAL PAPER

# Structural investigations of neodymium incorporation in calcium stannate perovskite $CaSnO_3$

Jules Goethals[1] · Chloé Fourdrin[1] · Martine Tarrida[1] · Ali Bedidi[1] · Frédéric Hatert[2] · Stéphanie Rossano[1]

Received: 13 March 2018 / Accepted: 13 July 2018


## Abstract

Samples of calcium stannate perovskite ($CaSnO_3$) doped with a variable Nd content were synthesized by solid-state reaction in the system $(1-x)CaSnO_3-xNd_2O_3$. The synthesized compounds were characterized by means of electron microprobe, powder X-ray diffraction, single-crystal X-ray diffraction and μ-Raman spectroscopy. The incorporation of Nd in the $CaSnO_3$ *Pbnm* structure leads to the formation of a complex $(Ca_{1-2x}\,Nd_{2x})(Sn_{1-x}Ca_x)O_3$ perovskite. The A sublattice contains a random distribution of Ca and Nd in the whole range of composition of this system. For $x<0.28$, the structure is *Pbnm* with Ca and Sn randomly distributed in the B sublattice. For $x>0.28$ a symmetry change occurs; the structure turns into rock salt type $P2_1/n$. In this latter case half of the octahedral sites are fully occupied by Sn and the other half is randomly occupied by Sn and Ca. For $x=0.28$, both structures are present in the sample. The presence of a Raman two modes behavior of $A_{1g}$ symmetry located near 700 $cm^{-1}$ coupled with the continuous linear evolution of the lattice parameters with Nd incorporation supports the proposed substitution mechanism.

**Keywords** Perovskite · Calcium stannate · Neodymium · Raman spectroscopy · X-ray diffraction

## Introduction

Calcium stannate $CaSnO_3$, a dielectric material, has been extensively investigated for its potential use as capacitor (Azad et al. 1999), anode for Li-ion batteries (Zhao et al. 2010; Mouyane et al. 2011), gas and humidity sensors (Seiyama et al. 1983; Cerdà et al. 2002; Cheng and Lu 2008) and analogue for the Earth mantle perovskite (Zhao et al. 2004; Redfern et al. 2011; Maul et al. 2015). When doped with trivalent rare earth elements, $CaSnO_3$ may exhibit interesting luminescence properties, as for example, long afterglow luminescence (Lei et al. 2007; Pang et al. 2011; Canimoglu et al. 2015; Xie et al. 2016). The calcium stannate perovskite is also considered as an analogue (same *Pbnm* structure) to the calcium titanate and calcium zirconate perovskites that have been proposed as hosts for the disposal of long term radioactive wastes (Ringwood 1985). In these two latter structures, the incorporation of large $REE^{3+}$ is widely reported in the literature (Hanajiri et al. 1998; Davies et al. 2000; Larguem 2006; Zhang et al. 2007). However, the incorporation of a large amount of large $REE^{3+}$ in the calcium stannate perovskite has not been investigated to our knowledge. $ABO_3$ perovskites are in general flexible and can incorporate in their structure more than half of the elements of the Mendeleïev table (Mitchell 2002). Incorporation of trivalent cations in the $ABO_3$ perovskite structure results in an intricacy of the structure with various substitution mechanisms to assume charge balance. Large $REE^{3+}$ such as Nd, with an ionic radii of 1.27 Å in 12-fold coordination state (Shannon and Prewitt 1970), are supposed to replace $A^{2+}$ cation in $A^{2+}B^{4+}O_3$ perovskite and then behave as electron donors (Buscaglia et al. 2000).

In the case of an A site incorporation of $REE^{3+}$ in $CaTiO_3$, the following potential compensation charge mechanisms are reported in the literature (Kröger-Vink notations):

**Electronic supplementary material** The online version of this article (https://doi.org/10.1007/s00269-018-0993-7) contains supplementary material, which is available to authorized users.

✉ Jules Goethals
jules.goethals@u-pem.fr

[1] Université Paris-Est, LGE (EA 4508), UPEMLV, 77454 Marne-la-Vallée, France

[2] Laboratoire de Minéralogie, Université de Liège, B18, Allée du 6 août, 4000 Liège, Belgium

Published online: 27 July 2018

1. Substitution at calcium site with calcium vacancies compensation (Larson et al. 1988; Bassoli et al. 2008; Fu et al. 2008; Lowndes et al. 2012):

$$Ln_2O_3 + 3\,TiO_2 \overset{CaTiO_3}{\rightarrow} 3\,CaTiO_3 + 2\,Ln_{Ca}^{\cdot} + V_{Ca}''$$

2. Substitution at calcium site with titanium vacancies compensation (Larson et al. 1988; Bassoli et al. 2008):

$$Ln_2O_3 + \frac{3}{2}\,TiO_2 \overset{CaTiO_3}{\rightarrow} 2\,CaTiO_3 + 2\,Ln_{Ca}^{\cdot} + \frac{1}{2}\,V_{Ti}'$$

3. Substitution at calcium site with electron conduction (i.e., titanium reduction compensation) (Vance et al. 1996):

$$Ln_2O_3 + 2\,TiO_2 \overset{CaTiO_3}{\rightarrow} 2\,CaTiO_3 + 2\,Ln_{Ca}^{\cdot} + \frac{1}{2}O_2 + 2\,e^-$$

The aim of this study is to explore the substitution mechanisms involved in the system $(1-x)\,CaSnO_3 - xNd_2O_3$ while incorporating Nd, by solid-state reaction, in an already formed $CaSnO_3$ perovskite structure. These potential mechanisms were investigated by means of electron microprobe (EMPA), X-ray diffraction and ∝-Raman spectroscopy.

## Experimental

### Synthesis

$(1-x)CaSnO_3 - xNd_2O_3$ samples with different amount of neodymium oxide ranging from $x=0$ to $x=0.56$ were synthetized by a solid-state reaction route in two steps: $CaSnO_3$ synthesis followed by a Nd doping. The different precursors were $CaCO_3$ (Alfa Aesar, 99%), $SnO_2$ (Alfa Aesar, 99.9%) and $Nd(OH)_3$ formed by hydration of $Nd_2O_3$ (Alfa Aesar, 99%). The initial powders were first dried at 100 °C during at least 1 day. The $CaSnO_3$ synthesis was made starting from stoichiometric amounts of $CaCO_3$ and $SnO_2$. The mixture was ground in an agate mortar with a pestle before being calcined at 900 °C during 2 h and sintered in a Pt–Rh crucible at 1300 °C during 1 day. The obtained solids were then crushed and sintered again for another day. The Nd-doped samples were prepared by mixing the $CaSnO_3$ powder with neodymium hydroxide in an agate mortar. The mixtures were first sintered in Pt-Rh crucible at 1550 °C during one day, reground and sintered again at 1550 °C during 3 days. The obtained solids were reduced into powder to be analyzed by XRD.

In parallel, pellets of 3 mm in diameter with similar compositions were prepared to follow microstructural evolution upon Nd incorporation. In the latter case, appropriate mixture of $CaSnO_3$ and $Nd(OH)_3$ were ground in an agate mortar. The mixtures were then pressed and sintered in a Pt-Rh crucible during 3 days at 1550 °C.

To clarify notations, powdered and pelletized samples are named as *x*(value)pow and *x*(value)pel, respectively, with value standing for the molar % concentration of initial $Nd_2O_3$.

For electron microprobe and μ-Raman analyses, powdered and pelletized samples were embedded into resin and polished successively with 1200, 2400, 4000 grade SiC. The final polishing step was obtained using successively 3 and 1 μm diamond paste. For single-crystal XRD, two single-crystals of dimension 0.10 mm × 0.08 mm × 0.07 mm and 0.08 mm × 0.09 mm × 0.12 mm were extracted from samples ×35 pel and ×44 pel, respectively.

### Microprobe analysis and SEM imaging

Analysis and SEM imaging were done with a microprobe CAMECA SX-Five of the CAMPARIS facility in Paris. The accelerated electron beam was set to 15 keV, 40 nA for both analysis and imaging. The beam size for analysis was approximately 3 μm in diameter. LTAP (Si $K_\alpha$), PET (Ca $K_\alpha$, Sn $K_\alpha$, La $K_\alpha$), LPET (Nd $L_\alpha$) were used as diffracting crystals. Standards used, for calibration purposes, were: grossular for Si and Ca, cassiterite for Sn, $Nd_2CuO_4$ for Nd, $LaReO_4$ for La. Si and La were present in the form of impurities originating from the initial powders ($Nd_2O_3$, Alfa Aesar 99%). Analyses were done on ten different perovskite grains larger than 5 μm for each sample to characterize the perovskite compositions. Only one analysis was done per secondary phases observed in some samples.

### Powder XRD measurements

Powder XRD measurements were performed with a D8 Advance diffractometer equipped with a Lynx Eye detector (*Bruker*) operating at 40 keV and 40 mA in Bragg–Brentano geometry. The patterns were obtained with Co $K_\alpha$ radiation ($\lambda = 1.7889$ Å) in the 2θ range from 10° to 110° using a step of 0.009° during 2 h. The Soller slits were set at an aperture of 2.5°. The divergence and anti-diffusion slits were fixed, respectively, at 0.3° and 6.42° apertures. The lattice parameters were obtained by Le Bail refinement using the Fullprof suite (Carvajal 1990).

### Single-crystal XRD

Single-crystal X-ray structural study was carried out on a Rigaku Excalibur four-circle diffractometer with a Mo $K_\alpha$ radiation source ($\lambda = 0.71073$ Å) and equipped with an EOS CCD-area detector. Grains of ×35 pel and ×44 pel samples

were sufficiently coarse and optically free of defects. One grain of each sample was subjected to single-crystal diffraction analyses.

Frames with a 1° spatial resolution were collected by the $\varphi/\omega$ scan technique, with a counting time of 10 s per frame, in the range $8.55 < 2\theta < 57.95°$ (×35 pel) and $4.88 < 2\theta < 58.04°$ (×44 pel). A total of 1804 (×35 pel) and 2135 (×44 pel) reflections were extracted from these frames, corresponding to 631 (°35 pel) and 656 (°44 pel) unique reflections. Data were corrected for Lorentz-polarisation and absorption effects, the latter with an analytical method using the SCALE3 ABSPACK scaling algorithm included in the CrysAlisRED package (Oxford Diffraction 2007). More details on data collection, reduction, and structure refinement procedures are given in Table 1.

For each cationic crystallographic site, RSP (Refined Site Population) were refined using SHELL X 93 (Sheldrick 1993). The refinements were completed using anisotropic displacement parameters for all atoms.

The space group was determined using the most intense reflections and confirmed using the absent reflections.

## Raman spectroscopy

The Raman spectra were collected on the powdered and pelletized polished samples at room temperature with a µ-Raman Renishaw InVia equipped with a Leika DM2700M microscope. A Nd:YAG laser ($\lambda = 532$ nm) powered at 5 mW was used as incident monochromatic source. The set-up is further composed of a grating of 1800 lines/mm and a short distance objective lense ×100 (NA = 0.95) leading to a theoretical spot diameter of 0.7 µm. Calibration on silicon standard was done previous to acquisition. All the acquisitions were performed on ten different single grains for each sample to obtain standard deviation values. For each acquisition, spectra were collected 30 times during 1 s each. The scans were acquired from 60 to 1840 $cm^{-1}$. The $A_{1g}$ modes, modeled as gaussians, were fitted using the Wire™ software.

**Table 1** Experimental details for the single-crystal X-ray structure refinements

| | ×35 pel | ×44 pel |
|---|---|---|
| Crystal dimensions (mm) | 0.10 × 0.08 × 0.07 | 0.08 × 0.09 × 0.12 |
| $a$ (Å) | 5.6468 (3) | 5.6586 (3) |
| $b$ (Å) | 5.8796 (3) | 5.9171 (3) |
| $c$ (Å) | 8.1426 (4) | 8.1874 (5) |
| $\beta$ (°) | 90.071 (5) | 90.140 (5) |
| Space group | $P2_1/n$ | $P2_1/n$ |
| $Z$ | 4 | 4 |
| Diffractometer and operating conditions | Rigaku Xcalibur with EOS detector, 40 kV and 40 mA, Mo $K\alpha$ radiation, $\lambda = 0.71073$ Å | |
| Scan mode | ω scan | ω scan |
| $\theta_{min}$, $\theta_{max}$ | 4.28°, 28.97° | 2.44°, 29.02° |
| Range of indices | $-7 \le h \le 7$ | $-3 \le h \le 7$ |
| | $-7 \le k \le 6$ | $-7 \le k \le 8$ |
| | $-10 \le l \le 10$ | $-10 \le l \le 10$ |
| Measured intensities | 1804 | 2135 |
| Unique reflections | 631 | 656 |
| Independent non-zero [I > 2 s(I)] reflections | 583 | 604 |
| Absorption correction | Numeric, using a multifaceted crystal model | |
| $\mu$ ($mm^{-1}$) | 19.616 | 22.371 |
| Structure solution program | SHELXS-97 (Sheldrick 2008) | |
| l.s. refinement program | SHELXL-93 (Sheldrick 1993) | |
| Refined parameters | 51 | 51 |
| $R_1$ ($F_o > 2\sigma$ ($F_o$)) | 0.0428 | 0.0383 |
| $R_1$ (all) | 0.0455 | 0.0408 |
| $wR_2$ (all) | 0.1171 | 0.1019 |
| $S$ (goodness of fit) | 0.984 | 1.120 |
| Max $\Delta/\sigma$ in the last l.s. cycle | 0.000 | 0.000 |
| Max peak and hole in the final $\Delta F$ map ($e$/Å$^3$) | + 1.63 and − 6.19 | + 1.60 and − 5.24 |

## Results and discussion

### Microprobe analyses and SEM imaging

Microprobe analyses and SEM imaging were performed on the powdered and the pelletized samples. The major phase compositions for the powdered and the pelletized samples are reported in Table 2. We can remark the presence of Si and La impurities originating from the $Nd_2O_3$ precursor material.

The powdered and pelletized samples are mostly composed of the expected perovskite ($CaSnO_3$:Nd) although secondary minor phases were observed (see Table 3 for powdered samples).

Regarding the secondary phases, at low Nd values (below $x = 0.19$), the formation of a $Ca_2SnO_4$ phase containing a very low amount of Nd was evidenced in both powdered (Table 3) and pelletized samples (not shown). In the samples ×5 pel and ×8 pel, this phase is present as automorph lozenge or rectangular grains of several decades to hundreds of micrometers (Fig. 1), whereas grains of this phase are smaller and pseudomorphic in ×12 pel and ×16 pel. The concentration of this phase is decreasing with Nd incorporation as evidenced for the pelletized samples by the electron-backscattered images (Fig. 1). Beyond $x = 0.23$, this phase is not present.

At higher Nd values, in powdered samples (×37 pow, ×45 pow, ×56 pow), an exsolved phase rich in Nd, and containing Ca and Sn appears (for ×56 pow see Table 3). This phase is chemically heterogeneous and its composition varies within the samples (not shown). This exsolved phase appears to be visually more significant in ×56 pow.

Nevertheless, the major part of Nd is incorporated in the perovskite structure. According to the low calculated standard deviations, the perovskite compositions can be

**Table 2** Microprobe analysis of the samples given in atomic percentage

| Sample | $x$ | Si (at %) | Ca (at %) | Sn (at %) | Nd (at %) | La (at %) | Ca/Sn |
|---|---|---|---|---|---|---|---|
| ×4 pow | 0.043 (1) | 0.12 (5) | 18.75 (7) | 19.28 (8) | 1.72 (5) | 0.01 (1) | 0.972 (5) |
| ×9 pow | 0.091 (4) | 0.11 (1) | 17.79 (6) | 18.31 (11) | 3.62 (14) | 0.04 (1) | 0.969 (6) |
| ×12 pow | 0.123 (4) | 0.13 (2) | 17.18 (10) | 17.65 (11) | 4.88 (15) | 0.05 (1) | 0.970 (5) |
| ×19 pow | 0.186 (8) | 0.20 (3) | 15.93 (19) | 16.28 (17) | 7.40 (33) | 0.09 (1) | 0.976 (5) |
| ×23 pow | 0.233 (19) | 0.23 (2) | 15.07 (38) | 15.30 (40) | 9.21 (76) | 0.10 (2) | 0.983 (6) |
| ×28 pow | 0.279 (14) | 0.27 (1) | 14.09 (23) | 14.36 (35) | 11.04 (57) | 0.13 (2) | 0.981 (9) |
| ×33 pow | 0.327 (6) | 0.29 (2) | 13.20 (14) | 13.36 (12) | 12.89 (23) | 0.17 (1) | 0.986 (3) |
| ×37 pow | 0.371 (6) | 0.33 (1) | 12.30 (11) | 12.48 (15) | 14.61 (25) | 0.17 (2) | 0.983 (10) |
| ×45 pow | 0.450 (2) | 0.41 (1) | 11.06 (22) | 10.62 (10) | 17.70 (7) | 0.20 (2) | 1.032 (19) |
| ×56 pow | 0.451 (9) | 0.42 (1) | 11.34 (67) | 10.37 (22) | 17.76 (29) | 0.21 (3) | 1.093 (87) |
| ×5 pel | 0.047 (3) | 0.07 (1) | 18.74 (12) | 19.16 (12) | 1.91 (11) | 0.02 (1) | 0.982 (5) |
| ×8 pel | 0.084 (5) | 0.09 (1) | 18.07 (13) | 18.37 (13) | 3.35 (21) | 0.03 (1) | 0.984 (7) |
| ×12 pel | 0.123 (1) | 0.11 (1) | 17.27 (8) | 17.60 (5) | 4.88 (3) | 0.06 (1) | 0.981 (6) |
| ×16 pel | 0.160 (3) | 0.15 (1) | 16.53 (8) | 16.82 (9) | 6.35 (12) | 0.07 (2) | 0.982 (7) |
| ×22 pel | 0.219 (7) | 0.19 (1) | 15.30 (11) | 15.61 (18) | 8.67 (28) | 0.10 (2) | 0.979 (7) |
| ×28 pel | 0.276 (13) | 0.25 (5) | 14.36 (28) | 14.30 (29) | 10.91 (50) | 0.12 (2) | 1.004 (15) |
| ×29 pel | 0.285 (3) | 0.24 (1) | 14.04 (8) | 14.21 (9) | 11.28 (12) | 0.14 (1) | 0.989 (7) |
| ×35 pel | 0.349 (2) | 0.30 (1) | 12.74 (7) | 12.90 (8) | 13.78 (11) | 0.16 (1) | 0.988 (7) |
| ×44 pel | 0.438 (3) | 0.38 (1) | 10.96 (11) | 11.11 (10) | 17.21 (11) | 0.19 (1) | 0.986 (16) |

Measurements were performed on ten points. Each calculated value is given in the form: mean (standard deviation). $x$ is the molar concentration of $Nd_2O_3$

**Table 3** Microprobe analyses of the secondary phases observed in the powdered samples given in atomic percentage of element

| Sample | Si (at %) | Ca (at %) | Sn (at %) | Nd (at%) | La (at%) | O (at %) | Formula |
|---|---|---|---|---|---|---|---|
| ×4 pow | 0.05 | 28.06 | 14.35 | 0.29 | < DL | 57.27 | $Ca_2SnO_4$:Nd |
| ×9 pow | 0.04 | 27.90 | 14.18 | 0.63 | < DL | 57.26 | $Ca_2SnO_4$:Nd |
| ×45 pow | 0.88 | 4.33 | 1.31 | 33.41 | 0.38 | 59.55 | Unknown |
| ×56 pow | 0.87 | 2.04 | 1.91 | 34.56 | 0.39 | 59.88 | Unknown |

Measurements were performed on single points

*DL* detection limit

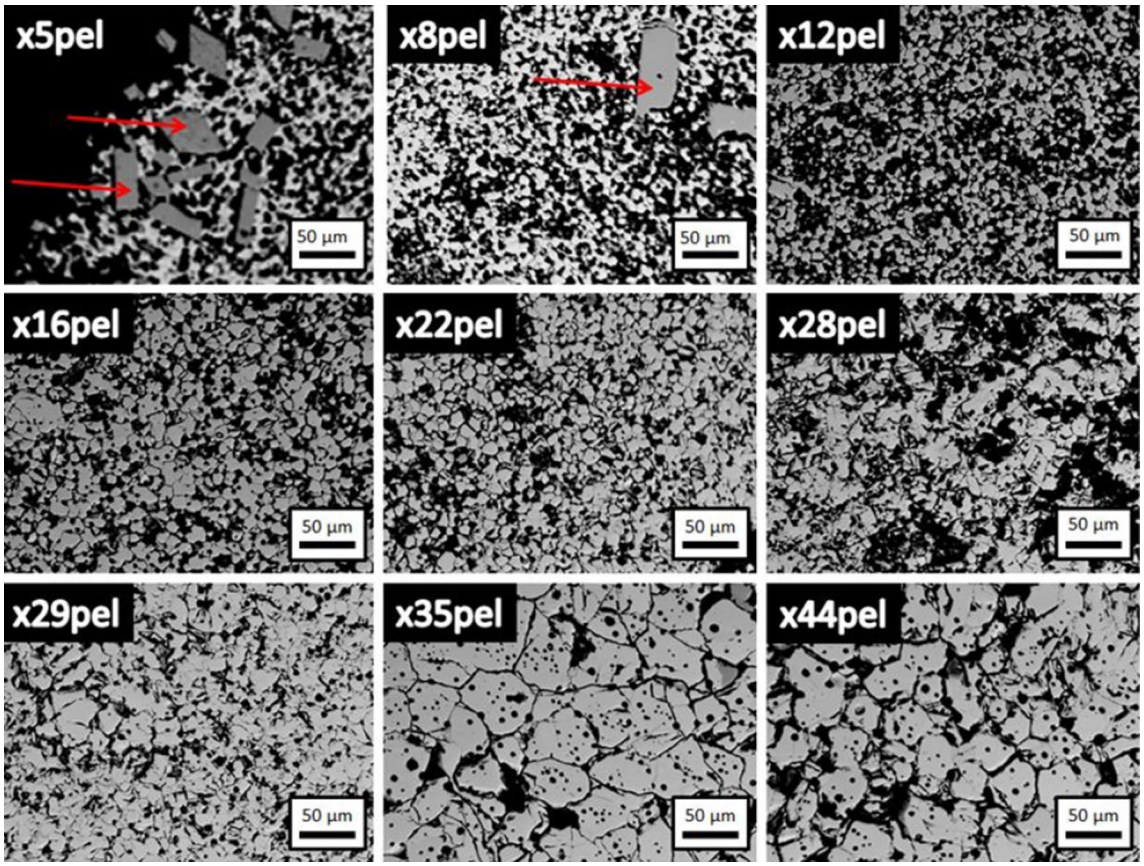


**Fig. 1** Backscattered electron images of the pelletized samples. Red arrows are pointing automorphic grains of $Ca_2SnO_4$

considered as homogeneous (Table 2). A quasi exponential increase of the grain size of the perovskite is observed with addition of Nd until ×35 pel (Fig. 2). A high-porosity of the samples, at low Nd concentration is observed and could be linked to the use of a hydroxide as precursor. However, a global decrease in the porosity occurs with increasing Nd content suggesting that grain growth is the main densification process. Grains do not present domain boundaries such as twins which are frequently observed in stannate perovskite (Vegas et al. 1986). The absence of this kind of defect could at least partially explain the high-grain growth rate (Fig. 1).

Besides, Ca/Sn ratios for all samples are given in Table 2. They are slightly lower than one at low Nd values and increase from $x = 0.45$ to $x = 0.56$. This increase could be related to the exsolution phenomenon.

## XRD measurements

The XRD patterns of the powdered samples $(1-x)CaSnO_3 - xNd_2O_3$ are shown in Fig. 3. For the initial $CaSnO_3$ sample, all the peaks were attributed to the orthorhombic phase $CaSnO_3$, as confirmed by comparison

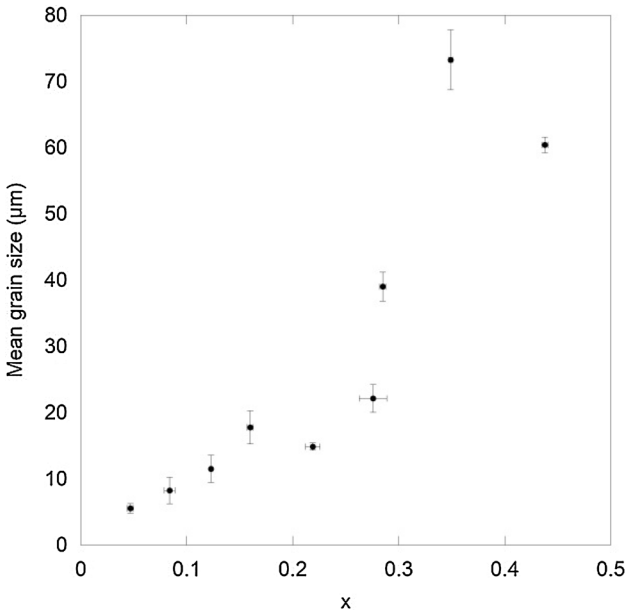


**Fig. 2** Mean grain size of the pelletized samples ($x$ value taken from Table 2) the standard deviation values were calculated from the measurements of the mean grain size on three different optical images (approximately 200 grains measured per image)

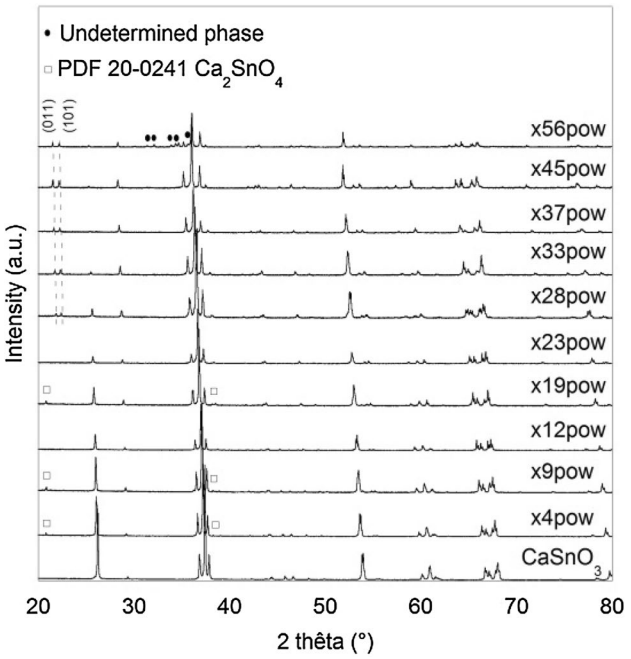


**Fig. 3** XRD patterns of the powdered samples

with PDF 31–0312. The refinement of the lattice parameters are consistent with those reported in the literature $a = 5.5142$ (2), $b = 5.6634$ (2), $c = 7.8816$ (2) (Zhao et al. 2004).

As observed in Fig. 3, the Nd incorporation induces a shift of the major peaks, corresponding to the perovskite phase, to lower 2θ° values. Besides, the secondary phases observed by EMPA, are detected by XRD when their concentration is sufficient. Indeed, $Ca_2SnO_4$ was observed in the samples ×4 pow, ×9 pow and ×19 pow. Reflections of the $Ca_2SnO_4$ phase are slightly shifted compared to the reference (PDF 20–0241) in accordance with incorporation of a small amount of Nd into this phase (Table 3).

The Nd rich exsolved phase was only detected in the sample ×56 pow. Although EMPA showed its presence in the ×45 pow and x37 pow samples, its low amount might have prevented its detection by conventional powder XRD. The major reflections superposition of this phase with the perovskite ones makes their distinction challenging and, therefore, its lattice parameters could not be refined.

Regarding the perovskite phase, from ×28 pow, two new superlattice reflections are observed at small angles signing a symmetry change. They were indexed as (011) and (101). These reflections are due to the loss of the *b* glide plane present in the *Pbnm* symmetry. These new refections can be indexed as ½(111) and ½(1–11) in a simplified pseudo cubic lattice with $a \approx a_{pc}\sqrt{2}$, $b \approx a_{pc}\sqrt{2}$ and $c \approx 2a_{pc}$. They arise from A or B site cation ordering along $\boldsymbol{k} = 1/2{<}111{>}_{pc}$, i.e., 1:1 rock salt ordering (Howard et al. 2003; King and Woodward 2010). However, rock salt ordering of the A sublattice is very uncommon in perovskites (Knapp and Woodward 2006). Thus competition of two different chemical species on B site is to consider.

To get more information about symmetry change in our perovskite system, the classification of perovskite with octahedral tilting given by Glazer (Glazer 1972) and by Howard and co-authors (Howard et al. 2003) for ordered double perovskites can be used. For the Pbnm space group, the tilt system is denoted as $a^-a^-c^+$.

The space group after symmetry change should respect the following conditions:

1. Exhibit an $a^-a^-c^+$ tilt system, as no reflections associated with octahedral tilting appeared or disappeared;
2. Should necessarily be a subgroup of Pbnm (loss of the *b* glide plane);
3. Should allow ordering along $\boldsymbol{k} = 1/2{<}111{>}_{pc}$.

Those conditions are satisfied for the space group $P2_1/n$ (regular setting $P2_1/_c$) which is a maximal isomorphic subgroup of *Pbnm* and which is frequently adopted by rock salt ordered $A_2B'B''O_6$ double perovskite (Vasala and Karppinen 2015). These conditions are also satisfied by the space group $P2_1$ which only occurs very rarely in doubly ordered $A'A''B'B''O_6$ perovskites (King and Woodward 2010).

Thus, the lattice parameters were refined in the *Pbnm* and $P2_1/n$ systems before and after the symmetry change, respectively (Table 4). At the transition, the β angle is slightly deviated from 90° and increase with the Nd incorporation. Le Bail refinements plots for the samples ×23 pow and ×37 pow are given in Fig. 4. These refinements (Bragg R Factors: 6.59 and 4.75) suggests that the space groups *Pbnm* and $P2_1/n$ are the right ones. As can be observed in Fig. 5, the lattice parameters increase linearly, showing the continuous expansion of the initial unit-cell even after the symmetry change.

In addition, the duplication of the hkl reflections for the sample ×28 pow suggests the coexistence of two structures (before and after symmetry change) in this sample. Figure 6 shows this duplication for the (112) reflection. Thus, two phases were considered in the Le Bail refinement for this sample (see Table 4).

## Single-crystal X-ray diffraction

The space group deduced from the systematic absences observed in samples ×35 pel and ×44 pel, is $P2_1/n$, which is in agreement with the discussion on the powdered XRD results. Thus, the crystal structures of those samples were refined in the $P2_1/n$ space group and further details on intensity data collection and refinement are reported in Table 1.

The refined unit-cell parameters and their standard deviations are given in Table 1. They fit the linear behavior obtained from powdered XRD. The $R_1$ values given in

**Table 4** Lattice parameters and unit-cell volume of the powdered samples

| Sample | *a* | *b* | *c* | *β* | Volume | Space group |
|---|---|---|---|---|---|---|
| $CaSnO_3$ | 5.51627 (5) | 5.66148 (5) | 7.88316 (7) | 90 | 246.193 (4) | *Pbnm* |
| ×4 pow | 5.53421 (5) | 5.68556 (5) | 7.91613 (7) | 90 | 249.082 (4) | |
| ×9 pow | 5.55479 (8) | 5.71413 (7) | 7.95325 (11) | 90 | 252.442 (6) | |
| ×12 pow | 5.56641 (5) | 5.73367 (5) | 7.97497 (7) | 90 | 254.529 (4) | |
| ×19 pow | 5.58686 (11) | 5.76759 (11) | 8.01521 (17) | 90 | 258.272 (9) | |
| ×23 pow | 5.60081 (11) | 5.79321 (11) | 8.04471 (16) | 90 | 261.024 (9) | |
| ×28 pow | 5.61851 (15) | 5.81156 (15) | 8.06738 (23) | 90 | 263.418 (20) | |
| ×28 pow | 5.61825 (22) | 5.82639 (14) | 8.08359 (27) | 90.054 (5) | 264.609 (38) | $P2_1/n$ |
| ×33 pow | 5.62854 (7) | 5.85049 (8) | 8.10561 (14) | 90.068 (2) | 266.916 (7) | |
| ×37 pow | 5.64180 (12) | 5.87666 (10) | 8.14657 (20) | 90.080 (2) | 270.099 (10) | |
| ×45 pow | 5.66030 (8) | 5.92389 (7) | 8.18665 (9) | 90.082 (1) | 274.507 (6) | |

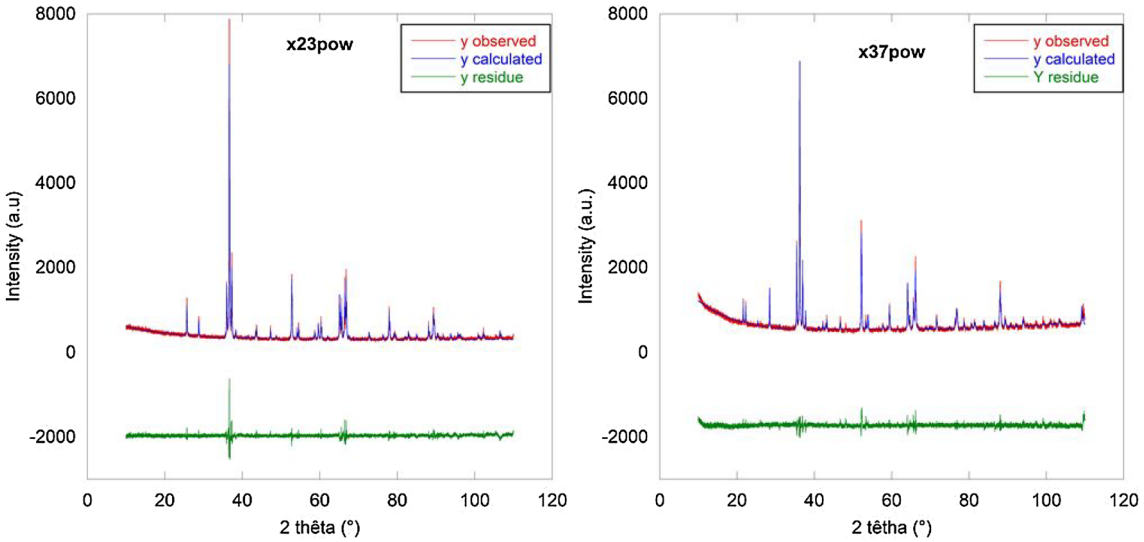


**Fig. 4** Le Bail refinements of the samples ×23 pow and ×37 pow

Table 1 are lower than 0.05 demonstrating a good structural determination for both samples. The high absolute value of holes in the final electron density map (Table 1) is induced by the presence of heavy atoms in these structures. In the $P2_1/n$ structure, A site atoms are in the 4e Wyckoff positions presenting the same multiplicity as the 4c Wyckoff position in the parent *Pbnm* structure, whereas B site (4b Wyckoff positions) of the *Pbnm* structure are splitted into 2a and 2b Wyckoff positions in the $P2_1/n$ structure, leading to the appearance of two distinctive B sites, denoted as B′ and B″. During the first step of the refinements, structures were refined with Nd and vacancies in the A site, Sn in the B′ (2a) site and Sn and vacancies in the B″(2b) site. Oxygens sites occupancies were fixed. The results of this first step are presented in the left column of Table 5. The detailed cationic distributions have been established by taking into account both the results of the chemical analyses and of the single-crystal structure refinements (Table 5). The obtained stoichiometry (EMPA) shows that the presence of vacancies is unexpected in this structure. Considering atomic numbers and the ionic radii of the principal cations (Nd, Sn and Ca) in our samples, the presence of Ca in A and B″ sites is mandatory. Indeed, the RSS value obtained for the B" site implies that this latter is also occupied by an atom presenting a lower Z value. Moreoverer, the difference of ionic radii between Ca (100 pm) and Sn (69 pm) in six-fold coordination state is significant (Shannon and Prewitt 1970) and explains the increase of the lattice volume with Nd incorporation observed by powdered XRD. Besides, as low amounts of Si and La are present in our samples, they have been attributed to B″ and A sites respectively according to their valences and their ionic radii. The cationic distribution assigned to the A, B′ and B″ sites is reported in the right column of Table 5. These results, are supported by the good agreement of the refined site populations (RSP), obtained from the single-crystal structure refinements, with

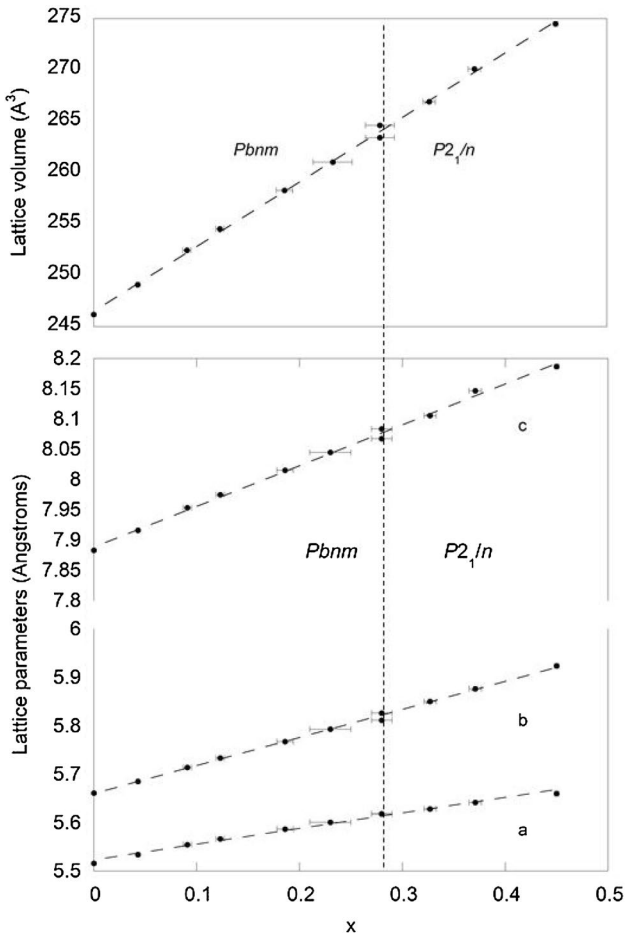


**Fig. 5** Lattice parameters obtained from the powdered samples. *x* values are determined from microprobe analysis (Table 2). The *y* esd values are within the marks

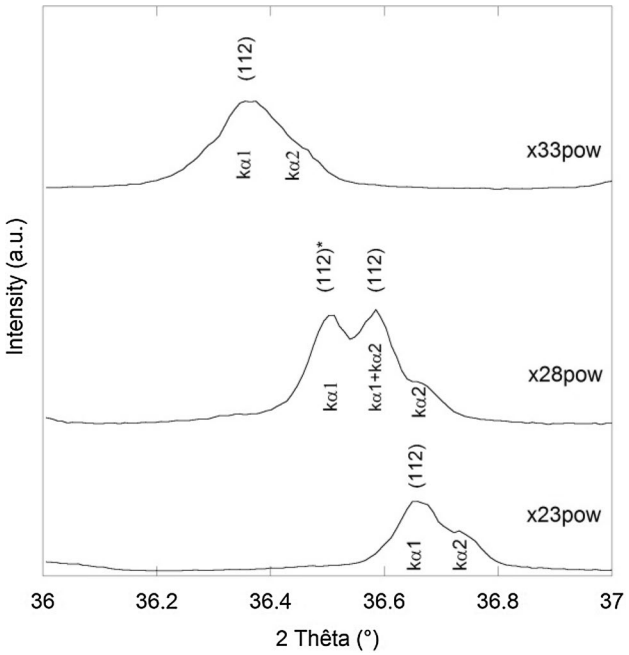


**Fig. 6** (112) reflection for the samples ×23 pow, ×28 pow and ×33 pow. The duplication of this reflection for the sample ×28 pow indicates the coexistence of two structures (before and after symmetry change). (*) Reflection of the phase after the symmetry change

the assigned site populations (ASP). Moreover, the refined site-scattering values (RSS) and the mean bond lengths (MBL), obtained from the structure refinements are very close to the calculated site-scattering values (CSS) and to the calculated bond lengths (CBL), respectively (Table 5). Finally, bond-valence sums (BVS), calculated, according to the expression $s = \exp[(R_0 - R)/0.37]$, using the $R_0$ values of Brown and Altermatt (1985) and the cation–oxygen bond lengths (Table 7), are close to the ideal bond-valence sums (IBVS) calculated from the assigned site population and cation valences.

To optimize these results, a second step with site occupancy factors refinement of Nd/Ca (A site) and Sn/Ca (B″ site) was performed.

Final atomic positions and nature, Wyckoff positions, equivalent displacement parameters and site occupancy factors (SOF) are given in Table 6. These final results are in very good accordance with the different results obtained in the first refinement step.

As a consequence of these findings, the following mechanism of substitution in ×35 pel and ×44 pel samples can be proposed:

$$(1-x)\mathrm{CaSnO_3} + x\mathrm{Nd_2O_3} \rightarrow \left(\mathrm{Ca_{1-2x}Nd_{2x}}\right)\left(\mathrm{Sn_{1-x}Ca_x}\right)\mathrm{O_3}$$

A crystallographic model representing this mechanism is presented in Fig. 7.

The bond length distortions (BLD) of a polyhedron can be determined using the following equation (Hatert et al. 2004):

$$\mathrm{BLD} = \frac{100}{n} \times \sum_{i=1}^{n} \frac{|d_i - d_m|}{d_m}$$

where $n$ is the number of interatomic distances, $d_i$ are the values of interatomic distances and $d_m$ is the mean value of the interatomic distances. The BLD deduced from the B′–O lengths (Table 7) are 0.68 and 0.63 for ×35 pel and ×44 pel respectively. For B″–O, they are of 0.20 and 0.66 for ×35 pel and ×44 pel respectively. These BLD are approximately 20 times superior to the Sn–O BLD of the $CaSnO_3$ structure reported by Zhao and co-authors (Zhao et al. 2004). These results mean that a distortion of the octahedral sites in addition with the $a^-a^-c^+$ tilting are necessary to accommodate the new substituted cations in the structure.

**Table 5** Refined site populations (RSP, APFU), refined site-scattering values (RSS, EPFU), mean bond lengths (MBL, Å), bond-valence sums (BVS, valence units), assigned site populations (ASP, APFU), calculated site-scattering values (CSS, EPFU), calculated bond lengths (CBL, Å), and ideal bond-valence sums (IBVS, valence units)

| Site | RSP | RSS | MBL[a] | BVS | ASP | CSS | CBL[b] | IBVS |
|---|---|---|---|---|---|---|---|---|
| ×35 pel | | | | | | | | |
| A | 0.790 (4) Nd + 0.21 | 47.4 | 2.585 | 2.27 | 0.301 Ca + 0.691 Nd + 0.008 La | 47.9 | 2.533 | 2.68 |
| B′ | 0.500 Sn | 50.0 | 2.072 | 3.83 | 0.500 Sn | 50.0 | 2.090 | 4.00 |
| B″ | 0.269 (3) Sn + 0.231 | 26.9 | 2.233 | 2.71 | 0.147 Sn + 0.338 Ca + 0.015 Si | 28.6 | 2.297 | 2.65 |
| ×44 pel | | | | | | | | |
| A | 0.903 (4) Nd + 0.097 | 54.2 | 2.589 | 2.58 | 0.126 Ca + 0.864 Nd + 0.010 La | 54.9 | 2.531 | 2.87 |
| B′ | 0.500 Sn | 50.0 | 2.069 | 3.86 | 0.500 Sn | 50.0 | 2.090 | 4.00 |
| B″ | 0.230 (3) Sn + 0.270 | 23.0 | 2.277 | 2.46 | 0.058 Sn + 0.424 Ca + 0.018 Si | 23.3 | 2.350 | 2.30 |

[a]The MBL have been determined considering eightfold and sixfold coordination state for the A and B site, respectively

[b]The CBL values have been calculated from the ASP with the effective ionic radii of Shannon and Prewitt (1970) considering eightfold and sixfold coordination state for the A and B site, respectively

**Table 6** Final atomic coordinates (*x, y, z*), Wyckoff positions, equivalent displacement parameter ($U_{eq}$) and site occupancy factor of the different atoms in the sample ×35 pel and ×45 pel

| Site | Atoms | *x* | *y* | *z* | Wyckoff position | $U_{eq}$ | *SOF* |
|---|---|---|---|---|---|---|---|
| ×35 pel | | | | | | | |
| A | Nd | 0.01572 (11) | 0.55709 (14) | 0.74853 (7) | 4e | 0.0093 (3) | 0.702 |
| A | Ca | 0.01572 (11) | 0.55709 (14) | 0.74853 (7) | 4e | 0.0093 (3) | 0.298 |
| B′ | Sn | 0 | 1 | 1 | 2a | 0.0072 (3) | 1 |
| B″ | Ca | 0 | 1 | 0.5 | 2b | 0.0045 (6) | 0.729 |
| B″ | Sn | 0 | 1 | 0.5 | 2b | 0.0045 (6) | 0.271 |
| O1 | O | 0.2020 (12) | 0.3160 (13) | 0.5555 (9) | 4e | 0.0162 (15) | 1 |
| O2 | O | −0.1166 (12) | 0.9488 (12) | 0.7602 (8) | 4e | 0.0131 (14) | 1 |
| O3 | O | 0.1807 (12) | 0.2938 (13) | 0.9342 (9) | 4e | 0.0170 (15) | 1 |
| ×44 pel | | | | | | | |
| A | Nd | 0.01661 (9) | 0.55769 (11) | 0.74799 (6) | 4e | 0.0091 (3) | 0.864 |
| A | Ca | 0.01661 (9) | 0.55769 (11) | 0.74799 (6) | 4e | 0.0091 (3) | 0.136 |
| B′ | Sn | 0 | 1 | 1 | 2a | 0.0059 (3) | 1 |
| B″ | Ca | 0 | 1 | 0.5 | 2b | 0.0060 (7) | 0.85 |
| B″ | Sn | 0 | 1 | 0.5 | 2b | 0.0060 (7) | 0.15 |
| O1 | O | 0.2026 (11) | 0.3189 (12) | 0.5566 (8) | 4e | 0.0110 (13) | 1 |
| O2 | O | −0.1229 (12) | 0.9433 (10) | 0.7645 (8) | 4e | 0.0138 (13) | 1 |
| O3 | O | 0.1768 (11) | 0.2928 (11) | 0.9299 (8) | 4e | 0.0143 (13) | 1 |

## Raman spectroscopy

The $CaSnO_3$ *Pbnm* unit-cell is composed of 20 atoms giving 54 points vibrational modes. Factor group analysis was done using the crystallographic Bilbao server (Aroyo et al. 2006, 2011) and leads to the following modes:

$$\Gamma(\mathrm{Pbnm}) = 8A_u + 10B_{1u} + 8B_{2u} + 10B_{3u} + 7A_g + 5B_{1g} + 7B_{2g} + 5B_{3g}$$

24 are Raman active: $7A_g + 5B_{1g} + 7B_{2g} + 5B_{3g}$. Among these modes there are four antisymmetric and two symmetric octahedral stretching modes, four bending modes and six octahedral rotation or tilt modes. The eight other modes are associated with the calcium cations (Redfern et al. 2011).

Raman spectra are reproduced in Fig. 8. For $CaSnO_3$, only 12 modes are experimentally observed (Fig. 8) in agreement with previous studies (McMillan and Ross 1988; Tarrida et al. 2009; Maul et al. 2015). The incorporation of Nd into the structure induces major changes in the spectra. As photoluminescence signal is overlapping the Raman signal at low frequencies (Orsi Gordo et al.

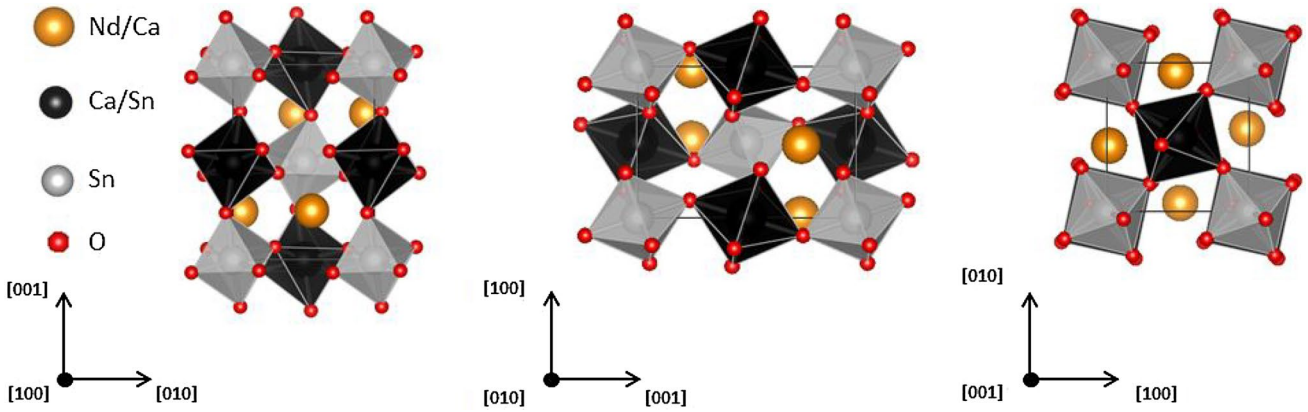


**Fig. 7** Crystallographic representation of the samples ×35 pel and ×44 pel along the 3 crystallographic directions. Graphics obtained using VESTA (Momma and Izumi 2011)

**Table 7** Final refined and mean cation–oxygen bond lengths (Å)

| | ×35 pel | ×44 pel |
|---|---|---|
| A–O1[a] | 2.862 (8) | 2.877 (7) |
| A–O1[a] | 2.720 (8) | 2.731 (7) |
| A–O1[a] | 2.364 (8) | 2.360 (7) |
| A–O2[a] | 2.423 (8) | 2.418 (7) |
| A–O2[a] | 2.343 (7) | 2.330 (7) |
| A–O3[a] | 2.946 (8) | 2.992 (7) |
| A–O3[a] | 2.664 (8) | 2.661 (7) |
| A–O3[a] | 2.355 (8) | 2.343 (7) |
| A–O2 | 3.453 (7) | 3.499 (7) |
| A–O1 | 3.769 (8) | 3.812 (7) |
| A–O2 | 3.655 (8) | 3.723 (6) |
| A–O3 | 3.791 (8) | 3.841 (7) |
| Mean[a] | 2.585 (2) | 2.589 (2) |
| B′–O1 (×2) | 2.051 (8) | 2.049(7) |
| B′–O2 (×2) | 2.082 (7) | 2.075 (7) |
| B′–O3 (×2) | 2.077(8) | 2.082 (7) |
| Mean | 2.073 (3) | 2.069 (2) |
| B″–O1 (×2) | 2.226 (8) | 2.255 (7) |
| B″–O2 (×2) | 2.240 (7) | 2.301 (7) |
| B″–O3 (×2) | 2.237 (8) | 2.274 (7) |
| Mean | 2.234 (3) | 2.277 (2) |

[a]Mean bond length of the A site are given for the eight A–O shortest distances

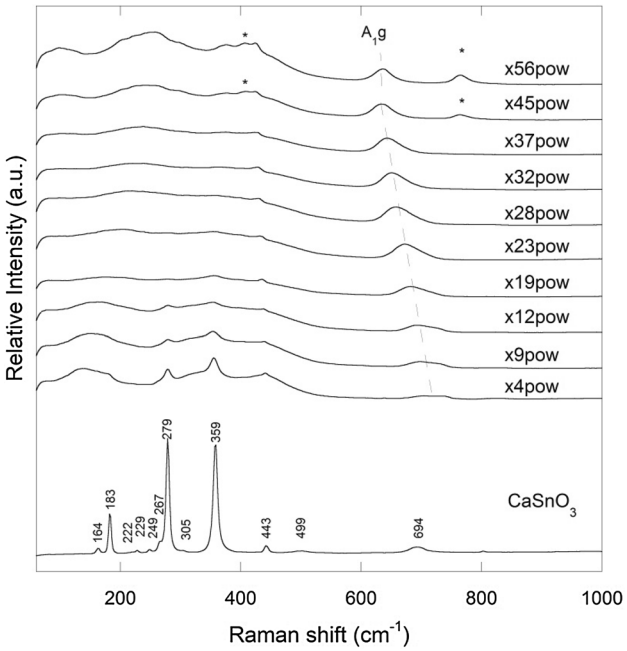


**Fig. 8** Raman spectra of the powdered samples. (*) indicate new bands appearing after exsolution

2015), this Raman study focuses on the high-frequency modes. As can be observed in Fig. 8, a broad band appears at approximately 700 $cm^{-1}$ as soon as Nd is incorporated. This band is frequently reported in complex perovskites, and is ascribed to an $A_{1g}$ octahedral breathing like mode of the oxygens. According to the literature, this band appears either when two cations of different size/valence are competing on the B site (Cairns et al. 2005), or in some A site doped perovskites presenting either A site vacancies (Lowndes et al. 2013), B site vacancies (Moraes et al. 2011) or oxygen vacancies (Animitsa et al. 2016). In any of the A site doping cases, the mode arises from local octahedral distortion and thus disruption of the long range ordering in the B sublattice.

Since the lattice parameters are following a continuous linear variation, we suggest that the mechanism proposed for sample ×35 pel and ×45 pel is also valid before the symmetry change. Therefore, in this study, the most probable explanation of this mode is the competition of Sn and Ca in the B site. In fully $A(B'B'')O_3$ disordered structures, this

mode corresponds to the vibration of the two different B site chemical species. Levin et al. (2006) reported this behavior for the $Ca(Zr_{1-x}Ti_x)O_3$ system. Thus, the $A_{1g}$ mode in our system was deconvoluted as a doublet of Gaussian curves representing the octahedral breathing modes of the $[CaO_6]$ and of their surrounding $[SnO_6]$ octahedra. The Gaussian distribution shape of the peaks can be due to structural/chemical disorder (e.g., distribution of local environment for the two types of octahedra). The obtained fits for the $A_{1g}$ band (×18 pow before and ×37 pow after symmetry change) are reported in Fig. 9 and variation of the frequency of the two modes as a function of Nd content are reported in Fig. 10. Before the symmetry change, the two frequencies exhibit the same trend, i.e., a parallel decrease with the Nd incorporation. However, after the symmetry change, the two frequencies become close. The two modes have almost the same frequency when the *x* content reached 0.45 in the perovskite. For this *x* value, the ratio Ca/Sn in the B site is almost 1. The proximity of the two bands might suggest a coupling of the $[CaO_6]$ and the $[SnO_6]$ octahedral breathing modes.

The results for the samples ×28 pow and ×28 pel show a greater dispersion over the ten measurements leading to greater error bars. This is due to the simultaneous presence of both *Pbnm* and $P2_1/n$ structures as shown by X-ray powder diffraction on ×28 pow sample.

Too insure that the $A_{1g}$ octahedral breathing modes were entirely due to a chemical effect, the intensity ratio of the two bands versus the Nd concentration was plotted (Fig. 11). Before symmetry change, intensity ratio versus x content is approximately following a linear trend. This is supporting the two modes behavior (i.e., two phonons modes with the same symmetry, but corresponding to two different chemical species). The increase of the intensity ratio is due to the increase of Ca content in the B site. Thus the contribution of the $[CaO_6]$ breathing mode increases with Nd incorporation. At symmetry change, intensity ratio drops abruptly. This can be attributed to the partial ordering of the B sublattice and so to the coupling of the two modes. Again, the coexistence

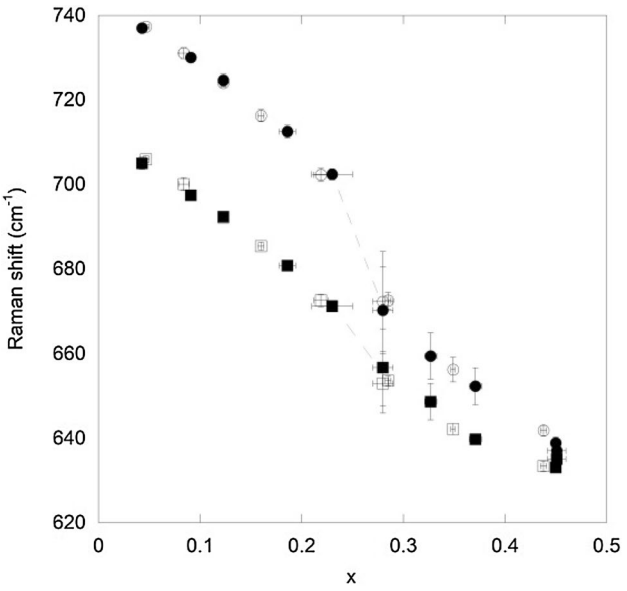


**Fig. 10** Frequencies of the $A_{1g}$ modes around the $[CaO_6]$ octahedra (squares) and their surrounding $[SnO_6]$ octahedra (circles). The x content (Table 2) is given by the EMPA results for the pelletized samples (white) and for the powdered samples (black). Standard deviations are calculated from ten spectra

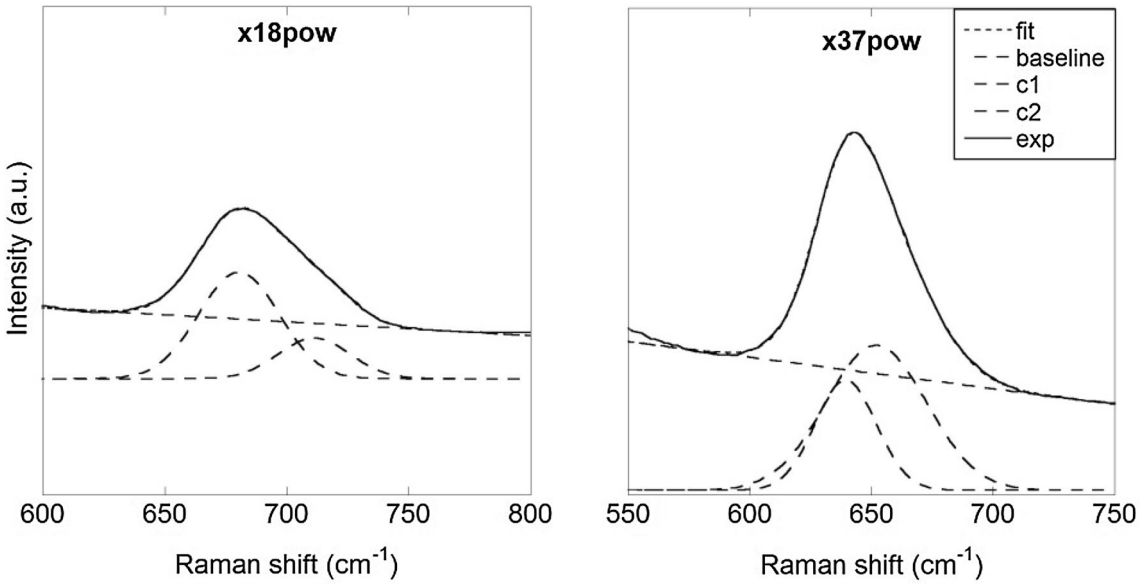


**Fig. 9** $A_{1g}$ modes fits of the samples ×18 pow and ×37 pow

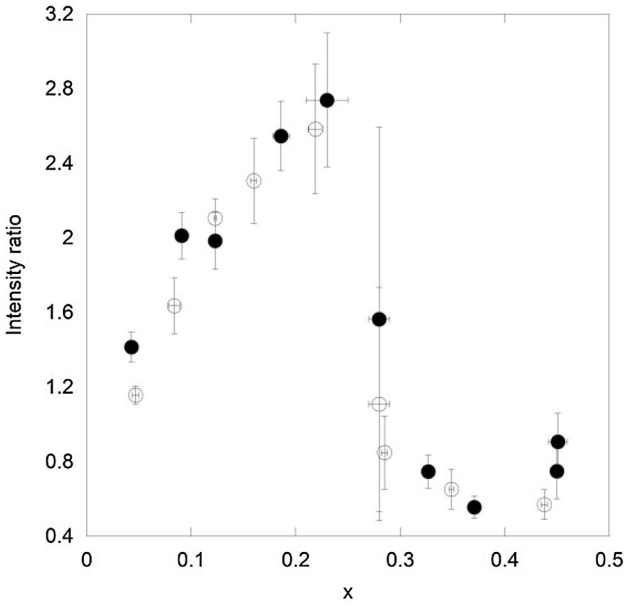


**Fig. 11** Intensity ratio of the $A_{1g}$ modes around the [$CaO_6$] octahedra and their surrounding [$SnO_6$] octahedra. The $x$ content (Table 2) is given by the EMPA results for the pelletized samples (white circles) and for the powdered samples (black circles). Standard deviations are calculated from ten spectra

of two different structures in the ×28 pel and ×28 pow samples leads to a wide dispersion of the intensity ratio for this $x$ value. An increase of the intensity ratio is observed after the exsolution phenomenon.

Hence, both frequency and intensity evolutions suggest that the $A_{1g}$ mode is entirely linked to the Ca and Sn competition on the B site. Furthermore, this is consistent with the substitution mechanism which is not involving vacancies. Besides, the proximity between the charge and size of Nd and Ca on the A site would lead to a very weak local distortion of the [$SnO_6$] octahedra compared to the one induced by the replacement of Sn by Ca in the B sublattice. Those evolutions are also suggesting the absence of clustering in the B sublattice in the structure before the symmetry change.

## Conclusion

This study shows that a large amount of Nd, up to 17% atomic (Table 2) can be hosted in the calcium stannate perovskite structure. In the frame of our synthesis protocol, we showed that trivalent Nd can be incorporated inside the perovskite structure without the need to create vacancies to counterbalance the excess of charges. The following mechanism of incorporation of Nd in $CaSnO_3$ can be proposed:

$$(1-x)CaSnO_3 + xNd_2O_3 \rightarrow \left(Ca_{1-2x}Nd_{2x}\right)\left(Sn_{1-x}Ca_x\right)O_3$$

It was supported by powder XRD, single-crystal XRD, EMPA and Raman spectroscopy.

This mechanism reveals an heterovalent coupled substitution of two $Nd^{3+}$ replacing two $Ca^{2+}$ in the A site while one $Ca^{2+}$ replaces one $Sn^{4+}$ in the B site. From $x \approx 0.28$, a symmetry change occurs; the structure turns from *Pbnm* to $P2_1/n$. After the symmetry change, the migration of Ca into the B site leads to a splitting of the B site into B′ and B″, leading to a double perovskite with a $P2_1/n$ structure. Single-crystal XRD supported the proposed mechanism for $x > 0.28$, while a continuous linear evolution of the lattice parameters and μ-Raman spectroscopy supported it for $x < 0.28$. Indeed, the high frequency $A_{1g}$ mode was assigned to the two different chemical types of octahedra. The frequencies and intensities behavior associated with the continuous linear evolution of the lattice parameters comfort this substitution mechanism before the symmetry change.

**Acknowledgements** The authors are thankful to M. Fialin (Centre de Microanalyses Camparis, Université Pierre et Marie Curie, Paris VI) for his help with the electron microprobe, J-D Mertz (LRMH) and M. Duc (IFSTTAR) for their help with DRX, O. Majérus (IRCP) for her help with Raman Spectroscopy; and B. Mihailova, G. Wallez, F. Guyot for their stimulating discussions.

## References

Animitsa I, Iakovleva A, Belova K (2016) Electrical properties and water incorporation in A-site deficient perovskite $La_{1-x}Ba_xNb_3O_{9-0.5x}$. J Solid State Chem 238:156–161. https://doi.org/10.1016/j.jssc.2016.03.023

Aroyo MI, Kirov A, Capillas C et al (2006) Bilbao Crystallographic Server. II. Representations of crystallographic point groups and space groups. Acta Cryst A 62:115–128. https://doi.org/10.1107/S0108767305040286

Aroyo MI, Perez-Mato JM, Orobengoa D et al (2011) Crystallography online: bilbao crystallographic server. Bulg Chem Commun. https://doi.org/10.1107/S205327331303091X

Azad AM, Shyan LLW, Alim MA (1999) Immittance response of $CaSnO_3$ prepared by self-heat-sustained reaction. J Mater Sci 34:1175–1187. https://doi.org/10.1023/A:1004596519893

Bassoli M, Buscaglia MT, Bottino C et al (2008) Defect chemistry and dielectric properties of $Yb^{3+}$: $CaTiO_3$ perovskite. J Appl Phys 103:14104. https://doi.org/10.1063/1.2828149

Brown ID, Altermatt D (1985) Bond-valence parameters obtained from a systematic analysis of the inorganic crystal structure database. Acta Crystallogr B41:244–247

Buscaglia MT, Buscaglia V, Viviani M et al (2000) Influence of foreign ions on the crystal structure of $BaTiO_3$. J Eur Ceram Soc 20:1997–2007. https://doi.org/10.1016/S0955-2219(00)00076-5

Cairns DL, Reaney IM, Zheng H et al (2005) Synthesis and characterization of $La(Co_{1/2}Ti_{1/2})O_3$. J Eur Ceram Soc 25:433–439. https://doi.org/10.1016/j.jeurceramsoc.2004.02.016

Canimoglu A, Garcia-Guinea J, Karabulut Y et al (2015) Cathodoluminescence properties of rare earth doped $CaSnO_3$ phosphor. Appl Radiat Isot 99:138–145. https://doi.org/10.1016/j.apradiso.2015.02.026

Carvajal JR (1990) FULLPROF: a program for Rietveld refinement and pattern matching analysis. In: Abstract of the Satellite Meeting on

Powder Diffraction of the XV Congress of the IUCr, Toulouse, France, 1990, p 127
Cerdà J, Arbiol J, Dezanneau G et al (2002) Perovskite-type $BaSnO_3$ powders for high temperature gas sensor applications. Sens Actuators B Chem 84:21–25. https://doi.org/10.1016/S0925-4005(02)00005-9
Cheng H, Lu Z (2008) Synthesis and gas-sensing properties of $CaSnO_3$ microcubes. Solid State Sci 10:1042–1048. https://doi.org/10.1016/j.solidstatesciences.2007.11.001
Davies RA, Islam MS, Chadwick AV, Rush GE (2000) Cation dopant sites in the $CaZrO_3$ proton conductor: a combined EXAFS and computer simulation study. Solid State Ionics 130:115–122. https://doi.org/10.1016/S0167-2738(00)00573-7
Fu MS, Liu XQ, Chen XM (2008) Structure and microwave dielectric characteristics of $Ca_{1-x}Nd_{2x/3}TiO_3$ ceramics. J Eur Ceram Soc 28:585–590. https://doi.org/10.1016/j.jeurceramsoc.2007.06.015
Glazer AM (1972) The classification of tilted octahedra in perovskites. Acta Crystallogr Sect B Struct Crystallogr Cryst Chem 28:3384–3392. https://doi.org/10.1107/S0567740872007976
Hanajiri Y, Matsui T, Harita Y et al (1998) EXAFS analyses of $CaTiO_3$ doped with Ce, Nd and U. Solid State Ionics 108:343–348. https://doi.org/10.1016/S0167-2738(98)00061-7
Hatert F, Long GJ, Hautot D et al (2004) A structural, magnetic, and Mössbauer spectral study of several Na-Mn-Fe-bearing alluaudites. Phys Chem Miner 31(8):487–506
Howard CJ, Kennedy BJ, Woodward PM (2003) Research papers Ordered double perovskites ± a group-theoretical analysis research papers. Acta Cryst B 59:463–471. https://doi.org/10.1107/S0108768103010073
King G, Woodward PM (2010) Cation ordering in perovskites. J Mater Chem 20:5785. https://doi.org/10.1039/b926757c
Knapp MC, Woodward PM (2006) A-site cation ordering in $AA'BB'O_6$ perovskites. J Solid State Chem 179:1076–1085. https://doi.org/10.1016/j.jssc.2006.01.005
Larguem H (2006) Évolution structurale et réactivité chimique hors et sous irradiation de céramiques oxydes envisagées pour le confinement spécifique de radionucléides à vie longue. Université de Marne La Vallée
Larson EM, Eller PG, Purson JD et al (1988) Synthesis and structural characterization of $CaTiO_3$ doped with 0.05–7.5 mole% gadolinium(III). J Solid State Chem 73:480–487. https://doi.org/10.1016/0022-4596(88)90134-X
Lei B, Li B, Zhang H, Li W (2007) Preparation and luminescence properties of $CaSnO_3$:$Sm^{3+}$ phosphor emitting in the reddish orange region. Opt Mater (Amst) 29:1491–1494. https://doi.org/10.1016/j.optmat.2006.07.011
Levin I, Cockayne E, Lufaso MW et al (2006) Local structures and Raman spectra in the $Ca(Zr,Ti)O_3$ perovskite solid solutions. Chem Mater 18:854–860. https://doi.org/10.1021/cm0523438
Lowndes R, Azough F, Cernik R, Freer R (2012) Structures and microwave dielectric properties of $Ca_{(1-x)}Nd_{2x/3}TiO_3$ ceramics. J Eur Ceram Soc 32:3791–3799. https://doi.org/10.1016/j.jeurceramsoc.2012.05.024
Lowndes R, Deluca M, Azough F, Freer R (2013) Probing structural changes in $Ca_{(1-x)}Nd_{2x/3}TiO_3$ ceramics by Raman spectroscopy. J Appl Phys 113:044115. https://doi.org/10.1063/1.4789601
Maul J, Erba A, Santos IMG et al (2015) In silico infrared and Raman spectroscopy under pressure: the case of $CaSnO_3$ perovskite. J Chem Phys. https://doi.org/10.1063/1.4905143
McMillan P, Ross N (1988) The Raman spectra of several orthorhombic calcium oxide perovskites. Phys Chem Miner 16:21–28. https://doi.org/10.1007/BF00201326
Mitchell RH (2002) Perovskites: modern and ancient. Almaz Press, Moscow
Momma K, Izumi F (2011) "VESTA 3 for three-dimensional visualization of crystal, volumetric and morphology data. J Appl Crystallogr 44:1272–1276
Moraes APA, Filho GS, Freire PTC et al (2011) Structural and optical properties of rare earth–doped $(Ba_{0.77}Ca_{0.23})1-x(Sm, Nd, Pr, Yb)xTiO_3$. J Appl Phys 109:124102. https://doi.org/10.1063/1.3594710
Mouyane M, Womes M, Jumas JC et al (2011) Original electrochemical mechanisms of $CaSnO_3$ and $CaSnSiO_5$ as anode materials for Li-ion batteries. J Solid State Chem 184:2877–2886. https://doi.org/10.1016/j.jssc.2011.08.038
Orsi Gordo V, Tuncer Arslanli Y, Canimoglu A et al (2015) Visible to infrared low temperature luminescence of $Er^{3+}$, $Nd^{3+}$ and $Sm^{3+}$ in $CaSnO_3$ phosphors. Appl Radiat Isot 99:69–76. https://doi.org/10.1016/j.apradiso.2015.02.019
Oxford Diffraction (2007) CrysAlis CCD and CrysAlis RED, version 1.71. Oxford Diffraction, Oxford
Pang XL, Jia CH, Li GQ, Zhang WF (2011) Bright white upconversion luminescence from $Er^{3+}$-$Tm^{3+}$-$Yb^{3+}$ doped $CaSnO_3$ powders. Opt Mater (Amst) 34:234–238. https://doi.org/10.1016/j.optmat.2011.08.019
Redfern ST, Chen C-J, Kung J et al (2011) Raman spectroscopy of $CaSnO_3$ at high temperature: a highly quasi-harmonic perovskite. J Phys Condens Matter 23:425401. https://doi.org/10.1088/0953-8984/23/42/425401
Ringwood AE (1985) Disposal of high-level nuclear wastes: a geological perspective. Mineral Mag 49:159–176. https://doi.org/10.1180/minmag.1985.049.351.04
Seiyama T, Yamazoe N, Arai H (1983) Ceramic humidity sensors. Sens Actuators 4:86–96
Shannon RD, Prewitt CT (1970) Revised values of effective ionic radii. Acta Crystallogr Sect B Struct Crystallogr Cryst Chem. https://doi.org/10.1107/S0567740870003576
Sheldrick GM (1993) *SHELXL93*. Program for the Refinement of Crystal Structures. University of Göttingen, Göttingen
Sheldrick GM (2008) A short history of SHELX. Acta Crystallogr A64:112–122
Tarrida M, Larguem H, Madon M (2009) Structural investigations of $(Ca,Sr)ZrO_3$ and $Ca(Sn,Zr)O_3$ perovskite compounds. Phys Chem Miner 36:403–413. https://doi.org/10.1007/s00269-008-0286-7
Vance E, Day R, Zhang Z et al (1996) Charge compensation in Gd-doped CaTiO3. J Solid State Chem 124:77–82. https://doi.org/10.1006/jssc.1996.0210
Vasala S, Karppinen M (2015) $A_2B'B''O_6$ perovskites: a review. Prog Solid State Chem 43:1–36. https://doi.org/10.1016/j.progsolidstchem.2014.08.001
Vegas A, Vallet-Regí M, González-Calbet JM, Alario-Franco MA (1986) The $ASnO_3$ (A = Ca, Sr) Perovskites. Acta Crystallogr Sect B Struct Sci 42:167–172. https://doi.org/10.1107/S0108768186098403
Xie J, Shi Y, Zhang F, Li G (2016) $CaSnO_3$:$Tb^{3+}$, $Eu^{3+}$: a distorted-perovskite structure phosphor with tunable photoluminescence properties. J Mater Sci 51:7471–7479. https://doi.org/10.1007/s10853-016-0021-6
Zhang Z, Lumpkin GR, Howard CJ et al (2007) Structures and phase diagram for the system $CaTiO_3$–$La_{2/3}TiO_3$. J Solid State Chem 180:1083–1092. https://doi.org/10.1016/j.jssc.2007.01.005
Zhao J, Ross NL, Angel RJ (2004) Tilting and distortion of $CaSnO_3$ perovskite to 7 GPa determined from single-crystal X-ray diffraction. Phys Chem Miner 31:299–305. https://doi.org/10.1007/s00269-004-0391-1
Zhao S, Bai Y, Zhang W-F (2010) Electrochemical performance of flowerlike $CaSnO_3$ as high capacity anode material for lithium-ion batteries. Electrochim Acta 55:3891–3896. https://doi.org/10.1016/j.electacta.2010.02.018